Constraints on spatially oscillating sub-mm forces from the Stanford Optically Levitated Microsphere Experiment data

I. Antoniou[1,*] and L. Perivolaropoulos[2,†]

[1]*Department of Physics, University of Ioannina, GR-45110 Ioannina, Greece*
[2]*Department of Physics, University of Patras, 26500 Patras, Greece*

(Received 15 August 2017; published 3 November 2017)

A recent analysis by one of the authors [L. Perivolaropoulos, Phys. Rev. D **95**, 084050 (2017)] has indicated the presence of a 2σ signal of spatially oscillating new force residuals in the torsion balance data of the Washington experiment. We extend that study and analyze the data of the Stanford Optically Levitated Microsphere Experiment (SOLME) [A. D. Rider *et al.*, Phys. Rev. Lett. **117**, 101101 (2016)] (kindly provided by A. D. Rider *et al.*) searching for sub-mm spatially oscillating new force signals. We find a statistically significant oscillating signal for a force residual of the form $F(z) = \alpha\cos(\frac{2\pi}{\lambda}z + c)$ where z is the distance between the macroscopic interacting masses (levitated microsphere and cantilever). The best fit parameter values are $\alpha = (1.1 \pm 0.4) \times 10^{-17}N, \lambda = (35.2 \pm 0.6)\ \mu$m. Monte Carlo simulation of the SOLME data under the assumption of zero force residuals has indicated that the statistical significance of this signal is at about 2σ level. The improvement of the χ^2 fit compared to the null hypothesis (zero residual force) corresponds to $\Delta\chi^2 = 13.1$. There are indications[1] that this previously unnoticed signal is indeed in the data but is most probably induced by a systematic effect caused by diffraction of non-Gaussian tails of the laser beam. Thus the amplitude of this detected signal can only be useful as an upper bound to the amplitude of new spatially oscillating forces on sub-mm scales. In the context of gravitational origin of the signal emerging from a fundamental modification of the Newtonian potential of the form $V_{\rm eff}(r) = -G\frac{M}{r}(1 + \alpha_O\cos(\frac{2\pi}{\lambda}r + \theta)) \equiv V_N(r) + V_{\rm osc}(r)$, we evaluate the source integral of the oscillating macroscopically induced force. If the origin of the SOLME oscillating signal is systematic, the parameter α_O is bounded as $\alpha_O < 10^7$ for $\lambda \simeq 35\ \mu$m. Thus, the SOLME data cannot provide useful constraints on the modified gravity parameter α_O. However, the constraints on the general phenomenological parameter α ($\alpha < 0.3 \times 10^{-17}N$ at 2σ) can be useful in constraining other fifth force models related to dark energy (chameleon oscillating potentials etc.).

DOI: 10.1103/PhysRevD.96.104002

I. INTRODUCTION

The physical scale associated with the accelerating expansion of the Universe is the dark energy scale which is obtained from the dark energy density $\rho_{\rm de} \simeq 10^{-29}\ {\rm g/cm^3} \simeq (2.4\ {\rm meV})^4$. This scale corresponds to an energy scale of 2.4 meV and a length scale of about $\lambda_{\rm de} \simeq \sqrt[4]{\frac{\hbar c}{\rho_{\rm de}}} = 0.085$ mm. It is therefore plausible that the physical cause of the cosmological expansion on cosmological scales may also produce experimental signatures in the form of new forces that manifest themselves on sub-mm scales. Chameleon scalar field screened interactions [1–8], modified gravity Yukawa forces [9,10] and vacuum energy Casimir forces [11–13] are some examples of new sub-mm forces that could also be connected with the observed cosmological accelerating expansion.

A wide range of experiments have been performed searching for signatures of new forces on sub-mm scales. They include torsion balance experiments [14–28], Casimir force experiments [29–31], levitating microsphere experiments [32–36], atomic interferometry [37] etc. These experiments as well as astrophysical observations on larger scales [38] fit particular parametrizations to data sets that usually involve force or torque residuals as function of separation between interacting bodies.

Parametrizations that are commonly used to model the spatial dependence of new forces on sub-mm scales are monotonic and include Yukawa and power law parametrizations [39]. Yukawa parametrizations generalize the gravitational potential generated by a mass M to the form

$$V_{\rm eff} = -G\frac{M}{r}(1 + \alpha_Y e^{-r/\lambda}) \tag{1.1}$$

where α_Y, λ are parameters to be constrained by the data. Power law parametrizations generalize the gravitational potential generated by a mass M to the form

*ianton@uoi.gr
†leandros@uoi.gr
On leave from the Department of Physics, University of Ioannina, 45110 Ioannina, Greece.

[1]Private communication with the authors of [2].

$$V_{\rm eff} = -G\frac{M}{r}\left(1+\beta^k\left(\frac{\lambda}{r}\right)^{k-1}\right) \tag{1.2}$$

where β, k are parameters. These parametrizations are motivated by viable extensions of general relativity (Brans-Dicke and scalar-tensor theories [40–42] brane world modes [43–48], $f(R)$ theories [49–51], compactified extra dimension models [52–58]. Alternative more complicated parametrizations which may not appear in closed analytic form are obtained in the context of nonrelativistic, steady-state chameleon fields, that couple directly to matter density and can mediate screened new forces between macroscopic objects [32,59–61] which may even be significantly larger than gravity [59].

Recent studies [62–65] have pointed out that a new class of parametrizations describing spatially oscillating new forces on sub-mm scales is well motivated theoretically and viable experimentally. Such oscillating parametrizations may describe deviations of the gravitational force from a Newtonian force in a wide range of modified gravity theories [62], in theories involving small scale granularity of dark energy [66,67] and most importantly in nonlocal (infinite derivative) gravity theories [10,62–65, 68–73]. These theories can be free from singularities [70,71,74,75] (such as black holes) and instabilities [72,73,76], they can emerge from quantum effects [69] (such as light particle loops) and they do not need the existence of the cosmological constant Λ to interpret the cosmological observations [77]. They constitute a viable physical mechanism for the observed accelerating expansion of the Universe [78–81] while they predict specific signatures in the gravitationally light bending angle [82] testable by the Chandra X-ray Observatory.[2]

Oscillating force residuals are experimentally viable and mildly favored [62] according to current torsion balance experiments searching for new forces on sub-mm scales [14]. These parametrizations also emerge as analytic continuations of the Yukawa parametrization (1.1) and generalize the Newtonian gravitational potential as

$$\begin{aligned} V_{\rm eff} &= -G\frac{M}{r}\left(1+\alpha_O\cos\left(\frac{2\pi}{\lambda}r+\theta\right)\right) \\ &\equiv V_N(r)+V_{\rm osc}(r) \end{aligned} \tag{1.3}$$

where α_O, λ, θ are free parameters and the spatial wavelength λ is assumed to be of sub-mm scale for consistency with current experimental constraints. This type of parametrization leads to oscillating new forces of sub-mm wavelength of the form

$$\vec{F} = -\hat{r}\frac{GMm}{r^2}\left[1+\alpha_O\cos\left(\frac{2\pi}{\lambda}r+\theta\right) + \alpha_O\frac{2\pi}{\lambda}r\sin\left(\frac{2\pi}{\lambda}r+\theta\right)\right]. \tag{1.4}$$

In the case of interacting macroscopic bodies the gravitational potential energy (and therefore the gravitational force) can be obtained by integration of the oscillating potential energy correction term [source integral obtained from the potential $V_{\rm osc}$ Eq. (1.3)] over the volumes of the interacting bodies. Assuming macroscopic interacting masses M and m with a common density ρ, the corresponding potential energy source integral may be written as

$$\begin{aligned} V_{\rm osc}(r) = -G\alpha_O\int_{V_m} d^3r_m\rho(\vec{r}_m)\int_{V_M} d^3r_M\rho(\vec{r}_M) \\ \times\frac{\cos(\frac{2\pi}{\lambda}|\vec{r}_m-\vec{r}_M|+\theta)}{|\vec{r}_m-\vec{r}_M|}. \end{aligned} \tag{1.5}$$

As demonstrated in Sec. III the effective force obtained from the potential source integral (1.5) macroscopic cylinder of mass M interacting with a small mass m located at a distance z from one of its bases along its symmetry axis is well approximated for intermediate to large z as

$$\vec{F}(z) = A\cos\left(\frac{2\pi}{\lambda}z+c\right)\hat{z} \tag{1.6}$$

where c is a parameter. Oscillating sub-mm force residuals like (1.6) were shown in Ref. [62] to be consistent with current torsion balance experiments [14] and in fact to provide a somewhat better fit than the null hypothesis of zero force residuals.

In the present study we extend the analysis of Ref [62] by fitting the spatially oscillating force residual (1.6) to the data set of Stanford Optically Levitated Microsphere Experiment (SOLME) [32] involving force measurements on optically levitated microspheres as a function of its distance z from a gold-coated silicon cantilever. The residual force obtained after the subtraction of a best fit electrostatic background from the total measured force in units of fN for $z\in[25,235]$ μm is fit to the oscillating force residual parametrization of Eq. (1.6) and the quality of fit is compared to the null hypothesis of zero force residual. The analytic expression of the source integral (1.5) is also investigated and its quality of fit to the SOLME data is compared to the corresponding quality of fit of the simpler approximate form (1.6) and other monotonic parametrizations.

This work is organized as follows: in Sec. II we describe the Stanford Optically Levitated Micropshere Experiment (SOLME) [32] and the data set used in our analysis. We also present the analysis of the data set and compare the likelihood of the oscillating residual force parametrization (1.6) with the likelihood of the null hypothesis (absence of

[2]http://chandra.harvard.edu/.

any residual force). In Sec. III we derive analytical expression for the source integrals leading to the macroscopic residual forces corresponding to the potential between a cylinder and a small sphere. We compare the quality of fit (likelihood) of macroscopic Yukawa, oscillating and power law residuals. Finally, in Sec. IV we conclude, summarize our results and discuss possible prospects of the present work.

II. CONSTRAINTS ON A PHENOMENOLOGICAL OSCILLATING PARAMETRIZATION

The SOLME [32] uses optically levitated dielectric microspheres supported by the radiation pressure from a single upward pointing laser beam. The laser traps the microsphere in a high vacuum thus counterbalancing Earth gravity. Any additional force is assumed to be due to a gold-coated silicon cantilever, located in the same height with the microsphera. In order to minimize electrostatic background forces the trap and cantilever are shielded in a cubic container consisting of six gold-plated electrodes which are set to approximately equal potential as the cantilever. Despite of this shielding, the main background force remains of electrostatic origin. It emerges due to the interaction of the small but nonzero permanent electric dipole moment of the microspheres which couples to the electric field due to the small but nonzero potential difference fluctuations (< 30 mV) between the cantilever and shielding electrodes. Thus the best fit electrostatic background may be used to obtain the residual force data as the difference between the measured total force and the best fit electrostatic background force at a given microsphere-cantilever distance z. Thus for the magnitude of the residual force dF we have

$$dF \equiv F_{\text{measured}} - F_{\text{background}}. \tag{2.1}$$

The data set analyzed in the present study corresponds to the data shown in Fig. 3 of Ref. [32]. The data and the best fit electrostatic background were kindly provided by the members of the SOLME [32] after our request. This data set was obtained using three silica microspheres with the same radius $r = 2.5$ μm and mass $m = 0.13$ ng but different polarizabilities. Each microsphera was trapped in a high vacuum with pressure $P < 10^{-6}$ mbar and its position was measured by a position-sensitive photodiode using a laser beam.

The small unshielded electrostatic background forces are monotonic with the distance z between cantilever and microsphera and have been modeled and fit by the members of the SOLME as functions of the distance z between the cantilever and the microsphere. We have found that this background is very well fit by a parametrization of the form $F_B = a + b/r^{3/2}$ where a, b are appropriate parameters that depend on the polarizability of the interacting microsphere. Any new type of force would manifest itself as a statistically significant nonzero residual force beyond the modeled electrostatic background.

For each one of the three silica microsphere the residual force of Eq. (2.1) was obtained for 32 distances z between cantilever and microsphere in the distance range z from 25 μm up to $\sim$235 μm. The total of 96 values of these residual forces along with the corresponding distances z and their 1σ error is shown in Table I in the Appendix (32 values for each one of the three microsphere).

We fit the residual forces of the SOLME data derived from Eq. (2.1) using the oscillating parametrization of the form

$$dF(\alpha, \lambda, c, z) = \alpha \cos\left(\frac{2\pi}{\lambda} z + c\right) \tag{2.2}$$

where α, λ and c are parameters to be fit. We have used the parametrization (2.2) to minimize $\chi^2(\alpha, \lambda, c)$ defined as

$$\chi^2(\alpha, \lambda, c) = \sum_{j=1}^{N} \frac{(dF(j) - dF(\alpha, \lambda, c, z_j))^2}{\sigma_j^2} \tag{2.3}$$

where j refers to the jth data point as resulted from Eq. (2.1) and $dF(\alpha, \lambda, c, z_j)$ is the residual force parametrized by Eq. (2.2), for the same distance z_j between cantilever and microsphera, that corresponds to measured residual force $dF(j)$. Also N is the number of data points which is 96 for the full data set.

We found that, for the full data set, $\chi^2(\alpha, \lambda, c)$ is minimized for

$$\alpha = 0.011 \pm 0.004 \ fN \tag{2.4}$$

$$\lambda = 35.2 \pm 0.6 \ \mu\text{m} \tag{2.5}$$

$$c = 5.47 \pm 0.06 \text{ rad} \simeq 7\pi/4. \tag{2.6}$$

This value of the best fit phase c differs by about π from the corresponding best fit phase obtained in Ref. [62] when fitting the Washington experiment data to the same parametrization. The minimum value of χ^2 is $\chi^2(\alpha, \lambda, c) = 85.2$ compared to $\chi^2(0, \lambda, c) = 98.3$ corresponding to zero residual force ($dF = 0$). In Fig. 1 we show the (minimized with respect to α, c) $\chi^2(\alpha, \lambda, c)$ for the full data set as a function of the spatial wavelength λ. Clearly, there is a well pronounced minimum at the spatial wavelength $\lambda = 35.2$ μm.

The red horizontal line corresponds to the value of χ^2 of zero residual force $dF(\alpha = 0, \lambda, c, r_j) = 0$. The difference between zero force residual and best fit oscillating parametrization is $\delta\chi^2 = 13.1$. The 1σ and 2σ contours for the two parameters α, λ (fixing $c = 7\pi/4$) are shown in Fig. 2. These contours indicate that the zero residual $\alpha = 0$ line is about 3σ away from the best fit $\alpha = 0.01$. In Fig. 3 we show

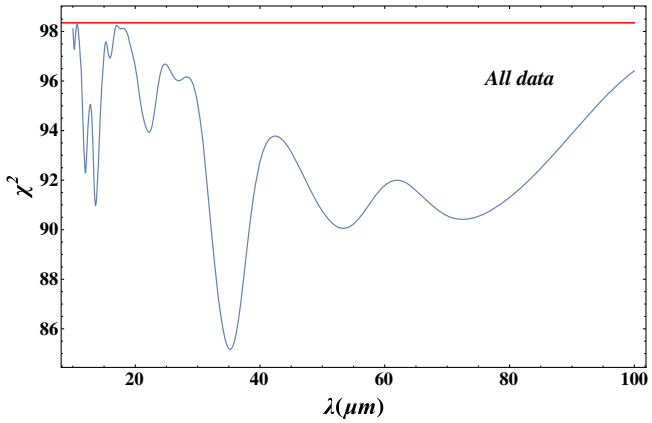

FIG. 1. The value of the minimized χ^2 as a function of the wavelength λ for the full data set (96 points). The red straight line corresponds zero residual force $dF = 0$. The depth of the minimum is $\delta\chi^2 = 13.1$.

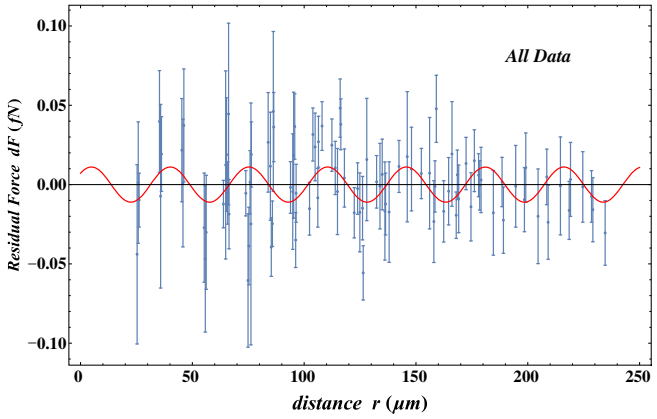

FIG. 3. The residual force SOLME data with error bars along with the best fit oscillating parametrization (thin red line) for the full data set. The best fit harmonic parametrization has spatial wavelength $\lambda = 35.2$ μm.

the full data set (residual force in fN vs distance in μm) along with the best fit oscillating model (2.2). The oscillating signal in the data is clearly visible.

In view of the presence of other less deep χ^2 minima at different spatial wavelengths, this 3σ estimate is an overestimate of the true significance of the oscillating signal. In order to estimate the correct statistical significance of the signal we have performed a Monte Carlo simulation. The goal of such a Monte Carlo simulation is to estimate how often would such a deep χ^2 minimum occur in SOLME simulated data derived under the assumption of an underlying zero residual force.

In order to verify the level of significance of the identified oscillating signal we have generated Gaussian Monte Carlo data sets under the assumption of zero residual force. In particular, we used the normal distribution to take random values for the residual forces (with mean value zero) for each data point distance z with the same standard deviation as the experimental data. We processed multiple data sets of random data points with the same method as the measured data. A typical form of $\delta\chi^2(\lambda) \equiv \chi^2_{\text{oscillating}} - \chi^2_{\alpha=0}$ (after minimization with respect to α, c at each value of λ) is shown in Fig. 4. Clearly, the depth of the deepest minimum of the Monte Carlo data set (red line) is significantly smaller than the maximum depth obtained with the real data set (blue line).

We considered 100 Monte Carlo zero residual force data sets and we calculated for each Monte Carlo data set the deepest χ^2 minimum in the range $\lambda \in [10\text{–}100]$ μm and subtracted this minimum χ^2 from the corresponding of zero

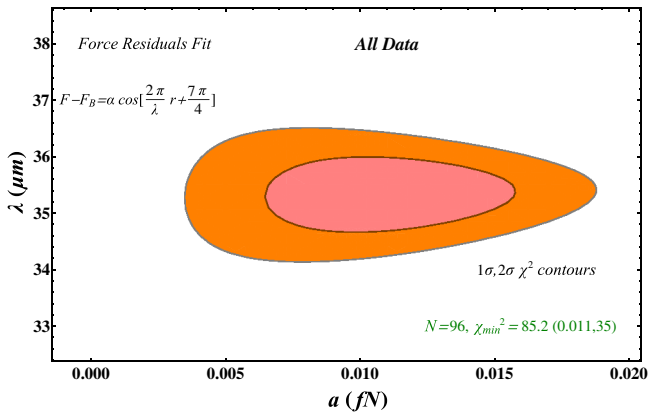

FIG. 2. The 1σ and 2σ contours in the parameter space (α, λ) for the oscillating parametrization with $c = 7\pi/4$. For the combined data set (96 data points) there is a well-defined high quality fit at $(\alpha, \lambda) = (0.011, 35.2\ \mu\text{m})$ corresponding to a wavelength $\lambda = 35.2$ μm. This best fit is about 3σ away from the zero force residual value $\alpha = 0$.

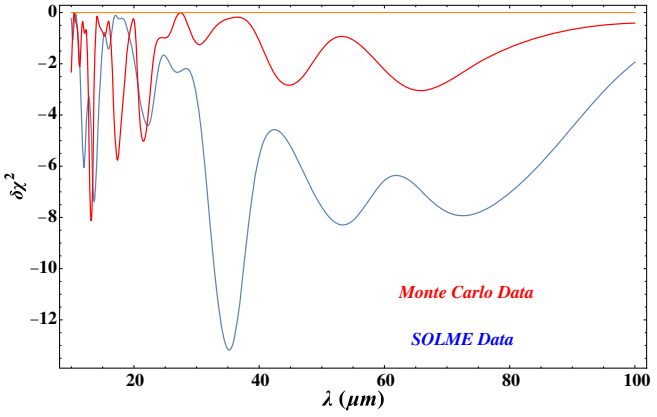

FIG. 4. The value of the minimized difference $\delta\chi^2 = \chi^2_{\text{oscillating}} - \chi^2_{\alpha=0}$ as a function of the spatial wavelength λ for the experimental data and a random Monte Carlo data set simulating the SOLME data under the assumption of zero residual force and gaussian errors. The depth of the $\delta\chi^2$ deepest minimum is significantly larger when the real data are fit to the oscillating parametrization.

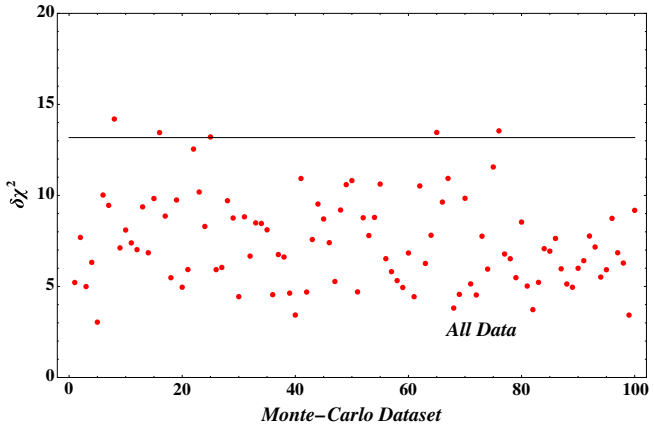

FIG. 5. The maximum $\delta\chi^2$ depth in the range $\lambda \in [10, 100]$ for 100 Monte Carlo data sets assuming zero residual force (red dots). The horizontal line corresponds to the maximum $\delta\chi^2$ depth for the actual SOLME data set.

residual force χ^2 obtained from the Monte Carlo data. Thus we calculated the difference

$$\delta\chi^2 = \chi^2_{\text{zero residual}} - \chi^2_{\text{min-oscillating residual}}. \tag{2.7}$$

For the real data this corresponds to the difference $\delta\chi^2$ between the $\alpha = 0$ red line of Fig. 1 and the deepest minimum of the blue line. This is the horizontal line in Fig. 5 at $\delta\chi^2 = 13.1$. For the Monte Carlo data sets this difference corresponds to the difference between the deepest minimum of the red line and the horizontal red line of Fig. 4. Each one of the red dots of Fig. 5 corresponds to such Monte Carlo difference. Clearly if all the 100 red dots were found below the horizontal line of Fig. 5 ($\delta\chi^2 < 13.1$) then there would be less than 1% probability that the deep χ^2 minimum of Fig. 1 is due to a statistical fluctuation. Instead we find that about 5% of the zero residual simulated data lead to deeper χ^2 minima (five red dots in Fig. 5 are above the horizontal line). Thus the true level of significance of the oscillating signal is at about 2σ. A similar effect leading to reduced level of significance compared to the one indicated by the χ^2 contour plot was observed and discussed in Ref. [62].

We conclude that there is evidence for an oscillating signal at the 2σ level in the SOLME data. Since there is only about 5% probability that this signal is due to a statistical fluctuation, most likely it is due either to a systematic effect that was not discussed in Ref. [32] or it is due to new physics. There are indications that the signal is most probably[3] due to a systematic effect caused by a background due to non-Gaussian tails of the laser beam whose pressure levitates the microsphere. Due to diffraction, the intensity of these non-Gaussian tails has a periodic oscillation, which can mimic a spatially oscillating force signal. Thus the amplitude of this detected signal can only be useful as an upper bound to the amplitude of new spatially oscillating forces on sub-mm scales.

In addition to the oscillating parametrization (2.2) we have tried to fit the data using various monotonic parametrizations like a Yukawa parametrization of the form

$$dF(\alpha, \lambda, z) = \alpha e^{z/\lambda}. \tag{2.8}$$

However, in all cases the improvement of the quality of fit was minor with $\delta\chi^2 < 1$ and thus we will not discuss these cases further in this section.

The oscillating parametrization (2.2) is a phenomenological parametrization which cannot be used as is to impose constraints on fundamental parameters. In order to impose such constraints the macroscopic residual force parametrization must be derived starting from a fundamental theory. For example we may assume a gravitational origin of the signal and derive the macroscopically induced residual force starting from a modified Newtonian potential of the form (1.3). Thus we may derive the predicted macroscopic residual force between cantilever and microsphere in terms of the fundamental parameters α_O and λ of Eq. (1.3) by evaluating the source integral (1.5) over the cantilever. This derived effective residual force may then be fit to the SOLME data leading to constraints on the fundamental parameters α_O and λ rather than the corresponding phenomenological parameters of Eq. (2.2). This task is undertaken in the next section.

III. CONSTRAINTS ON FUNDAMENTAL PARAMETERS: SOURCE INTEGRAL

A. Newtonian force between a cylindrical cantilever and a microsphere

We approximate the orthogonal cantilever of the SOLME by a cylindrical one of the same base area and height as the one used in the experiment. This allows for analytical evaluation of the source integral and of the macroscopic gravitational forces of the cantilever on the small microsphere located at a distance z along the symmetry axis from the center of the base of the cylindrical cantilever. Such a cantilever would have a radius $R \simeq 40\ \mu$m, height $L = 2000\ \mu$m (see Fig. 6) and density $\rho = 2.3 gr/\text{cm}^3$. As stated in the previous section the mass of the microsphere was $m = 0.13 ng$ and its radius $r = 2.5\ \mu$m.

We first calculate the Newtonian gravitational force between this cantilever and the microsphere. The gravitational potential energy between the cantilever and a point mass m at distance z from its surface is of the form

$$V_N(z) = -2\pi\rho G m \int_0^R r dr \int_z^{z+L} \frac{dz'}{\sqrt{r^2 + z'^2}} \tag{3.1}$$

[3]Private communication with the authors of [2].

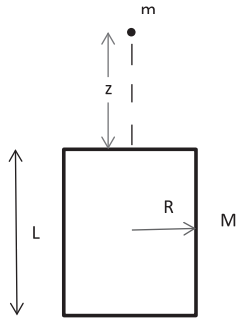

FIG. 6. The cantilever approximated as a cylinder and a point mass m at distance z from its surface.

We now introduce a rescaling to dimensionless length dividing all lengths by the cantilever radius R and denote with a 'bar' the new dimensionless quantities. Under this rescaling the potential (3.1) takes the form

$$V_N(\bar{z}) = -\underbrace{2\pi\rho G m R^2}_{V_1} \underbrace{\int_0^1 r' dr' \int_{\bar{z}}^{\bar{z}+\bar{L}} \frac{dz''}{\sqrt{r'^2+z''^2}}}_{\bar{V}_N(\bar{z})} \tag{3.2}$$

where the definitions of the potential unit V_1 and of the dimensionless gravitational potential $\bar{V}_N$ are shown in Eq. (3.2). The corresponding z component of the interaction force is

$$F_{zN}(\bar{z}) = -\underbrace{2\pi G m \rho R}_{F_1} \underbrace{\frac{\partial \bar{V}_N(\bar{z})}{\partial \bar{z}}}_{\bar{F}_{zN}(\bar{z})} \tag{3.3}$$

It is straightforward to calculate the dimensionless part of the force $\bar{F}_{zN}(\bar{z}) \equiv \frac{\partial \bar{V}_N(\bar{z})}{\partial \bar{z}}$ as

$$\bar{F}_{zN}(\bar{z},\bar{L}) = -\bar{L} - \sqrt{1+\bar{z}^2} + \sqrt{1+(\bar{L}+\bar{z})^2}. \tag{3.4}$$

For small $\bar{z}$ ($\bar{z} \ll 1$) this is a constant as expected

$$\bar{F}_{zN}(\bar{z},\bar{L}) \simeq \sqrt{1+\bar{L}} - (1+\bar{L}) \tag{3.5}$$

while for $\bar{z} \gg 1$ it also has the anticipated asymptotic behavior as an inverse square of the distance

$$\bar{F}_{zN}(\bar{z},\bar{L}) \simeq -\frac{\bar{L}}{2\bar{z}^2}. \tag{3.6}$$

The dimensions corresponding to the SOLME are $R = 40\,\mu$m, $\bar{L} = 50$, $\bar{r}_1 = 0.0625$, $\bar{z}_{\min} = 0.5$, $\bar{z}_{\max} = 6.25$ where $\bar{r}_1 \equiv \frac{r_1}{R}$ is the dimensionless form of the radius of the microsphere which is clearly much smaller than all the other dimensions of the experiment. In view of this fact we may approximate the microsphere as a point mass and assume that the predicted Newtonian force on it is provided to a good approximation by Eqs. (3.3) and (3.4).

An improved approximation for the calculation of the Newtonian force on the microsphere is the averaging of the force through the evaluation of the integral

$$\bar{F}_{zN,\text{total}}(\bar{z},\bar{L},\bar{r}_1) = \frac{1}{2\bar{r}_1}\int_{\bar{z}_0-\bar{r}_1}^{\bar{z}_0+\bar{r}_1} dz' \bar{F}_{zN}(z',\bar{L}). \tag{3.7}$$

We have found that this improved approximation has a minor effect (less than 1%) on the estimated force on the microsphere. Thus, in what follows we approximate the microsphere as a point mass that is subject to a Newtonian force from the cantilever provided by Eqs. (3.3) and (3.4) as

$$F_{zN}(\bar{z},\bar{L}) = \alpha_N \times \underbrace{2\pi G m \rho R}_{F_1} \times \bar{F}_{zN}\left(\frac{z}{40}, 50\right) \tag{3.8}$$

where z is in μm and $F_1 = 2\pi G m \rho R \simeq 5 \times 10^{-9} fN$ for the geometry and objects used in the SOLME. We have allowed for a short range amplification factor α_N to the Newtonian force. Since $\bar{F}_{zN}(\frac{z}{40}, 50) < 1$ for the distances considered in the SOLME ($z > 20\ \mu$m) it is clear that the Newtonian force is much smaller than the residual forces measured in the SOLME which are of $O(10^{-2}) fN$ and an amplification by a factor $\alpha_N \simeq 10^7$ on these scales would be required for such a force to be observable by the SOLME.

B. Yukawa and power law residual force between a cylindrical cantilever and a microsphere

Deviations from the Newtonian potential on submillimeter scales can be parametrized through a Yukawa interaction, an oscillating model or a power law parametrization. In the case of the Yukawa deviation, the potential energy of a point mass M interacting with a point mass m at a distance r gets generalized as $V(r) = V_N(r) + V_Y(r)$ with

$$V_Y(r) = -\frac{GMm}{r}\alpha_Y e^{-\frac{r}{\lambda}} \tag{3.9}$$

where α_Y and λ are appropriate parameters to be constrained. In this case, the Yukawa rescaled dimensionless interaction potential energy [see Eq. (3.1)] between a cylinder of dimensionless height $\bar{L}$ (the cantilever) and a point mass m (the microsphere) located at a distance $\bar{z}$ from the center of one of the cylinder bases is

$$\bar{V}_Y(\bar{z}) = -\alpha_Y \int_0^1 r' dr' \int_{\bar{z}}^{\bar{z}+\bar{L}} dz' \frac{e^{-\frac{\sqrt{r'^2+z'^2}}{\lambda}}}{\sqrt{r'^2+z'^2}}. \tag{3.10}$$

The corresponding z component of the force $\bar{F}_{zY}(\bar{z}) \equiv \frac{\partial \bar{V}_Y(\bar{z})}{\partial \bar{z}}$ induced on the mass m can be analytically evaluated by first obtaining the source integral (3.10) The result is

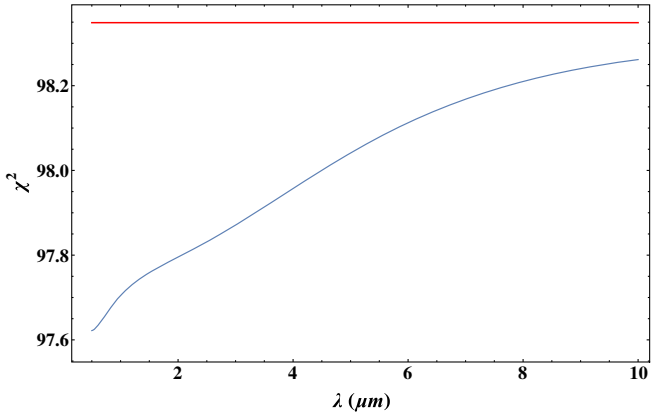

FIG. 7. The minimized χ^2 using the SOLME data as a function of the parameter λ of the Yukawa force ansatz including the effects of the source integral. The improvement of the fit is marginal despite the additional two parameters α_Y, λ.

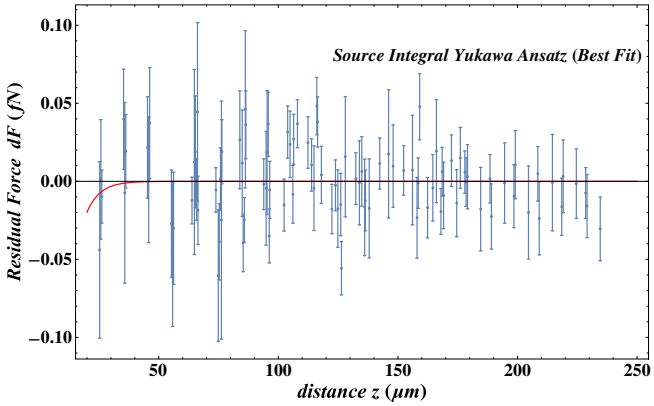

FIG. 8. The best fit form of the source integral for the Yukawa residual force is practically indistinguishable from the zero force residual.

$$\bar{F}_{zY}(\bar{z},\bar{L},\bar{\lambda}) = \alpha_Y \lambda \left(e^{-\frac{\bar{L}+\bar{z}}{\bar{\lambda}}} + e^{-\frac{\sqrt{1+\bar{z}^2}}{\bar{\lambda}}} - e^{-\frac{\bar{z}}{\bar{\lambda}}} - e^{-\frac{\sqrt{1+(\bar{L}+\bar{z})^2}}{\bar{\lambda}}} \right) \tag{3.11}$$

with $\bar{\lambda} = \frac{\lambda}{R}$. The asymptotic behavior of the macroscopic Yukawa force is as expected namely it is exponentially suppressed for $\bar{z} \gg 1$ while for small $\bar{z}$ it is constant approximated as

$$\bar{F}_{zY}(\bar{z},\bar{L},\bar{\lambda}) = \alpha_Y \bar{\lambda} \left(-1 + e^{-\frac{1}{\bar{\lambda}}} + e^{-\frac{\bar{L}}{\bar{\lambda}}} - e^{-\frac{\sqrt{1+\bar{L}^2}}{\bar{\lambda}}} \right). \tag{3.12}$$

For the SOLME the full residual Yukawa force may be expressed as

$$F_{zY,\mathrm{tot}} = \bar{F}_{zY,\mathrm{tot}}\left(\frac{z}{40}, 50, \frac{\lambda}{40}\right) \times 5 \times \underbrace{10^{-9} \times \alpha_Y}_{\alpha_{Y9}} \tag{3.13}$$

where z, λ must be substituted in μm and the force is in fN. We have found that as in the case of the simple phenomenological Yukawa parametrization discussed in the previous section, the source integral Yukawa force (3.13) is unable to improve the fit of the SOLME residual force data by more than 1 ($\delta\chi^2 < 1$) compared to the zero residual force parametrization. This is demonstrated in Fig. 7 where we show the minimum value of χ^2 as a function of λ for the macroscopic Yukawa force residual (3.13) and for the zero force residual (red line). Clearly we have $\delta\chi^2 < 1$ for all values of λ considered. Thus the Yukawa potential does not provide a more efficient macroscopic residual force parametrization for fitting the force residuals of the SOLME data compared to null hypothesis of the zero force residual. This is also demonstrated in Fig. 8 where we show the best fit Yukawa residual force for $\alpha_Y = 1$ which is achieved for $\lambda = 5.6\ \mu m$ and is practically indistinguishable from the zero residual force for most of the range of the force residual SOLME data.

A similar conclusion is obtained for other monotonic residual force parametrizations like power law deviations from the Newtonian potential. In that case the generalized gravitational potential would be of the form $V(r) = V_N(r) + V_P(r)$ with

$$V_P(r) = -\frac{\alpha_P G M m}{r^n}. \tag{3.14}$$

The rescaled dimensionless source integral may be written as

$$\bar{V}_P(\bar{z}) = -\alpha_P \int_0^1 r' dr' \int_{\bar{z}}^{\bar{z}+\bar{L}} \frac{dz'}{(r'^2 + z'^2)^{n/2}} \tag{3.15}$$

leading to the z component of the rescaled dimensionless force $\bar{F}_{zP}(\bar{z}) \equiv \frac{\partial \bar{V}_P(\bar{z})}{\partial \bar{z}}$ in the analytic form

$$\begin{aligned}\bar{F}_{zP}(\bar{z},\bar{L},n) = \alpha_P \frac{\bar{z}^{-n}(\bar{L}+\bar{z})^{-n}}{n-2}[(1+\bar{z}^2)[1+(\bar{L}+\bar{z})^2]]^{\frac{-n}{2}}\{-\bar{z}^n(\bar{L}+\bar{z})^n(1+\bar{z}^2)^{\frac{n}{2}}[1+(\bar{L}+\bar{z})^2] \\ + [1+(\bar{L}+\bar{z})^2]^{\frac{n}{2}}[\bar{z}^n(\bar{L}+\bar{z})^n(1+\bar{z}^2) + (1+\bar{z}^2)^{\frac{n}{2}}[\bar{z}^n(\bar{L}+\bar{z})^2 - \bar{z}^2(\bar{L}+\bar{z})^n]]\}.\end{aligned} \tag{3.16}$$

Introducing the parameters of the SOLME the dimensionful force in fN takes the form

$$F_{zP,tot} = \bar{F}_{zP,tot}\left(\frac{z}{40}, 50, n\right) \times 5 \times \underbrace{10^{-9} \times \alpha_P}_{\alpha_{Pg}}. \quad (3.17)$$

It is straightforward to show that the quality of fit of this power law source integral force residual is similar to that of the corresponding Yukawa residual and thus it is not of particular interest since it is not favored over the zero residual hypothesis. Thus we will not pursue this case further.

C. Oscillating force residual between a cylindrical cantilever and a microsphere

We now consider an oscillating gravitational residual potential of the form $V(r) = V_N(r) + V_O(r)$ with

$$V_O(r) = -\frac{GMm}{r}\alpha_O \cos\left(\frac{2\pi}{\lambda}r + \theta\right). \quad (3.18)$$

The macroscopic dimensionless form of the potential energy between a cylindrical cantilever and a microsphere on the cantilever's axis of symmetry is expressed in terms of the dimensionless source integral as

$$\bar{V}_O(\bar{z}) = -\alpha_O \int_0^1 r' dr' \int_{\bar{z}}^{\bar{z}+\bar{L}} dz' \frac{\cos\left(\frac{2\pi\sqrt{r'^2+z'^2}}{\lambda} + \theta\right)}{\sqrt{r'^2+z'^2}}. \quad (3.19)$$

The corresponding z component of the rescaled dimensionless force $\bar{F}_{zO}(\bar{z}) \equiv \frac{\partial \bar{V}_O(\bar{z})}{\partial \bar{z}}$, can be obtained analytically as

$$\begin{aligned}\bar{F}_{zO}(\bar{z}, \bar{L}, \bar{\lambda}, \theta) &= \frac{\alpha_O \bar{\lambda}}{2\pi}\left[\sin\left(\frac{2\pi\bar{z}}{\bar{\lambda}} + \theta\right) - \sin\left(\frac{2\pi(\bar{L}+\bar{z})}{\bar{\lambda}} + \theta\right)\right. \\ &+ \sin\left(\frac{2\pi\sqrt{1+(\bar{L}+\bar{z})^2}}{\bar{\lambda}} + \theta\right) \\ &\left. - \sin\left(\frac{2\pi\sqrt{1+\bar{z}^2}}{\bar{\lambda}} + \theta\right)\right]. \quad (3.20)\end{aligned}$$

For large z, the residual force (3.20) is oscillating with an amplitude that decreases as $1/\bar{z}$ and is of the form

$$\begin{aligned}\bar{F}_{zO}(\bar{z}, \bar{L}, \bar{\lambda}, \theta) = &\cos\left(\frac{2\pi\bar{z}}{\bar{\lambda}}\right)\frac{\cos\left(\frac{2\pi\bar{L}}{\bar{\lambda}} + \theta\right) - \cos\theta}{2\bar{z}} \\ &- \sin\left(\frac{2\pi\bar{z}}{\bar{\lambda}}\right)\frac{\sin\left(\frac{2\pi\bar{L}}{\bar{\lambda}} + \theta\right) - \sin\theta}{2\bar{z}}. \quad (3.21)\end{aligned}$$

For small $\bar{z}$ we find

$$\begin{aligned}\bar{F}_{zO}(\bar{z}, \bar{L}, \bar{\lambda}, \theta) &= \frac{\bar{\lambda}}{2\pi}\left[\sin\theta - \sin\left(\frac{2\pi}{\bar{\lambda}} + \theta\right) - \sin\left(\frac{2\pi\bar{L}}{\bar{\lambda}} + \theta\right)\right. \\ &\left. + \sin\left(\frac{2\pi\sqrt{1+\bar{L}^2}}{\bar{\lambda}} + \theta\right)\right]. \quad (3.22)\end{aligned}$$

For the case of the SOLME the oscillating residual force on the microsphere located at a distance $z\mu$m from the cantilever is would be of the form

$$F_{zO,\mathrm{tot}} = \bar{F}_{zO,\mathrm{tot}}\left(\frac{z}{40}, 50, \frac{\lambda}{40}, \theta\right) \times 5 \times \underbrace{10^{-9} \times \alpha_O}_{\alpha_{O9}} \quad (3.23)$$

where z, λ in μm and the force is in fN.

In Fig. 9 the force source integral (3.23) with $\lambda = 30$ μm and $\alpha_{O9} = 1$ (thick black dotted line) is compared with the plain harmonic residual force (2.2) with the same λ and $\alpha = 1$ (continuous red line), with the Newtonian source integral force (3.4) (long dashed line), with a power law source integral [$n = 1.5$, (3.16), blue dashed line] and with a Yukawa source integral force with $\lambda = 10$ μm (gray line). Notice that the oscillating force source integral for the particular parameters is an oscillating nonperiodic function with initially increasing amplitude which reaches a maximum and subsequently decreases at large distances in accordance with the predicted asymptotic behavior (3.21).

It is straightforward to fit the SOLME data using the macroscopic oscillating residual force (3.23) obtained from the source integral. In this case as in the case of the plain harmonic residual force (2.2) we have a significant improvement of the quality of fit compared to the zero

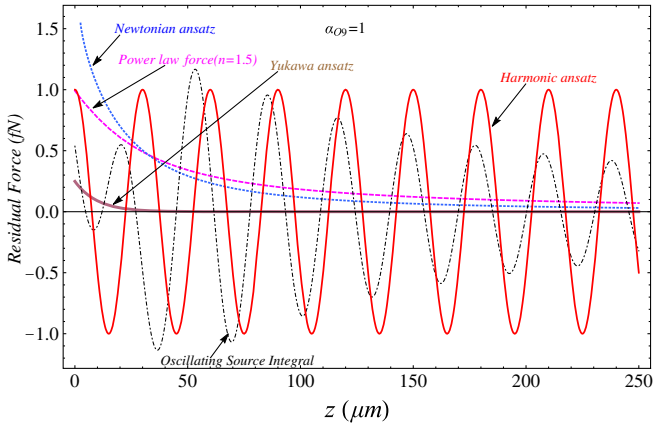

FIG. 9. Comparison between the source integral signal for oscillating force with the naive constant amplitude cosine oscillator. On scales z larger than the disk radius ($R = 40$ μm) they both behave like harmonic functions with very similar wavelength,while on small scales the signal is not periodic. Also, we have plot the Newtonian ansatz (blue line), the Yukawa ansatz (gray line) and a power law force with $n = 1.5$ (magenta line). For the oscillating source integrals we have set $\alpha_{O9} = 1$ which implies $\alpha_O = 10^9$.

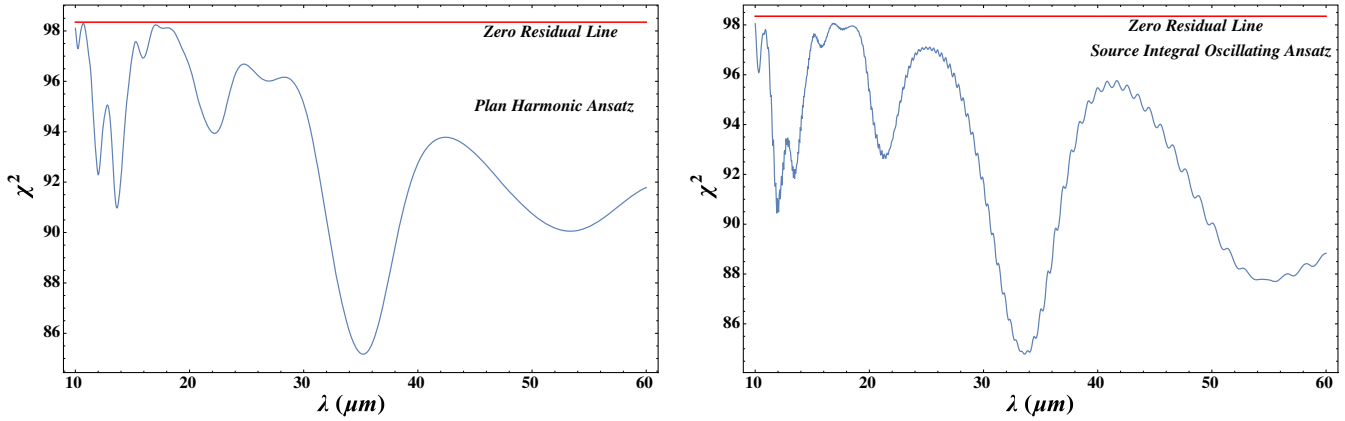

FIG. 10. Left panel: The χ^2 value as a function of the wavelength λ for plain harmonic ansatz. Right panel: The χ^2 value for the source integral oscillating ansatz. In both cases the fit improvement to the data is significant compared to a null residual fit. The difference in χ^2 is more than 13 units and the minimum appears in almost the same wavelength (about 35 μm).

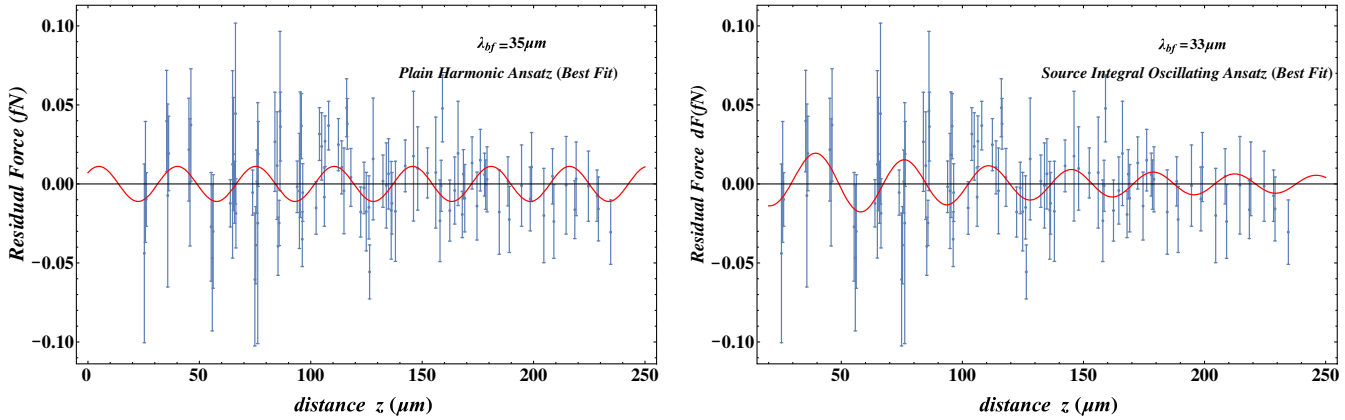

FIG. 11. Left panel: The best fit plain harmonic ansatz with $\lambda = 35$ μm. Right panel: The best fit source integral oscillating ansatz with $\lambda = 33$ μm. As we see, in both cases the waveform is practically the same even though the amplitude for the best fit source integral decreases slowly with distance.

residual hypothesis by $\delta\chi^2 > 13$. This is demonstrated in Fig. 10 (right panel) where we show the minimized χ^2 as a function of the spatial wavelength λ of the macroscopic oscillating force (3.23). The depth of the best fit χ^2 minimum is $\delta\chi^2 > 13$ and is obtained for $\lambda \simeq 33$ μm which is almost the same value $\lambda \simeq 35$ μm of the plain harmonic force parametrization (2.2) shown on the left panel[4]

In Fig. 11 (right panel) we show the best fit macroscopic oscillating force parametrization (3.23) superposed with the SOLME residual force data. For comparison we also show the corresponding best fit of the plain harmonic parametrization (2.2). The quality of fit (value of χ^2) is almost identical despite the fact that the right panel shows the full source integral best fit parametrization where the oscillation amplitude decreases slowly with z.

[4]The left panel of Fig. 10 is identical with Fig. 1 but we show it here again for easier comparison with the corresponding figure obtained using the full source integral (3.23) rather than the simple parametrization (2.2).

D. Oscillating source integral in cartesian coordinates

In order to make the evaluation of the source integral analytically tractable we have approximated the orthogonal cantilever used in the SOLME by a cylindrical one of the same base area. The orthogonal cantilever used in the SOLME had dimensions $a \times b \times L = 10$ μm $\times$ 500 μm $\times$ 2000 μm. Had we kept the orthogonal geometry in the evaluation of the oscillating force source integral and rescaled with the dimension $a = 10$ μm of the cantilever we would have to calculate the following source integral:

$$F_{Oz}(\bar{z}_0,\bar{\lambda},\theta) = Gm\rho a \times \alpha_O \times \frac{\partial}{\partial \bar{z}_0}\int_{-1}^{1} d\bar{x}\int_{-\bar{b}}^{\bar{b}} d\bar{y} \times \int_{\bar{z}_0}^{\bar{z}_0+\bar{L}} \frac{\cos\left(\frac{\sqrt{\bar{x}^2+\bar{y}^2+\bar{z}^2}}{\bar{\lambda}}+\theta\right)}{\sqrt{\bar{x}^2+\bar{y}^2+\bar{z}^2}} d\bar{z} \qquad (3.24)$$

which in contrast to the cylindrical geometry is not analytically tractable. Using a numerical approach we

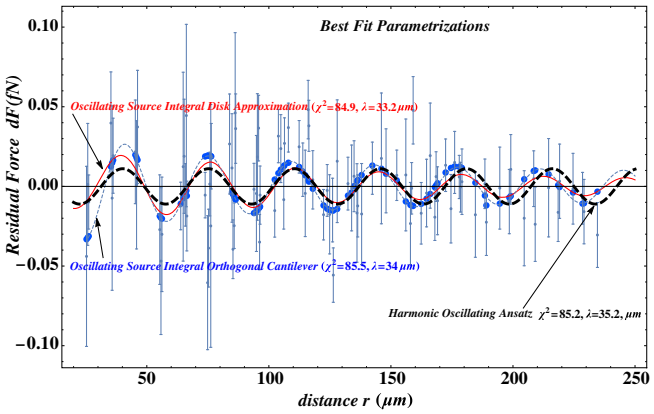

FIG. 12. The best fit source integrals for cylindrical (3.23) and orthogonal (3.24) cantilever along with the best fit plain harmonic force residual ansatz (2.2).The three best fit parametrizations are very similar leading to practically the same quality of fit.

have evaluated the source integral (3.24) at the distances of the data points and confirmed that a similar quality of fit can be obtained using the orthogonal source integral (3.24) as with the cylindrical analytic source integral (3.23) for the same spatial wavelength. Thus our result for the existence of the oscillating signal is robust and insensitive to the particular geometry used for the evaluation of the source integral. This is demonstrated in Fig. 12 where we show the best fit source integrals for cylindrical (3.23) and orthogonal (3.24) cantilever along with the best fit plain harmonic force residual ansatz (2.2). Clearly the three best fit parametrizations are very similar leading to practically the same quality of fit ($\chi^2 \simeq 85$) compared to the much lower quality of fit for the zero residual hypothesis and the Yukawa or power law residuals ($\chi^2 \simeq 98$).

IV. CONCLUSIONS-DISCUSSION

We have analyzed and fit the SOLME [32] force residual data using a wide range of parametrizations including plain phenomenological ones and parametrizations obtained by evaluating source integrals based on simple functional forms. We have shown that monotonic parametrizations (Yukawa and power laws) are unable to improve the quality of fit of the null hypothesis (zero force residuals) at any significant level despite the introduction of a number of parameters ($\delta\chi^2 < 1$). In contrast, oscillating parametrizations at the plain phenomenological level and at the level of source integral can improve significantly the quality of fit compared to the null hypothesis ($\delta\chi^2 > 13$). The statistical significance of this oscillating signal is at about 2σ level.

The most probable cause of this signal is a systematic effect caused by the non-Gaussian tails of the laser beam whose pressure levitates the microsphere. Due to diffraction, the intensity of these non-Gaussian tails has a periodic oscillation, which can mimic a spatially oscillating force signal. Thus the detected signal can only be used as an upper bound to physically interesting new forces of sub-mm oscillating nature. The amplitude α of such an oscillating force background with spatial wavelength $\lambda \simeq 35\ \mu$m is bounded at the 2σ level as $\alpha < 0.3 \times 10^{-17} N$. This bound is phenomenological and applicable to the conditions and geometry of the SOLME.

If the origin of this signal is assumed to be gravitational through a modified Newtonian potential of the form of Eq. (1.3) the bounds obtained on the parameter α_O are particularly weak ($\alpha_O < 10^7$) due to the partially shielded electrostatic backgrounds that limit the sensitivity of the experiment in measuring gravitational forces between the cantilever and the microsphere.

More interesting bounds on fundamental fifth force parameters could be obtained if the origin of the signal is assumed to be nongravitational. In particular, it is plausible that a chameleon potential with multiple extrema can lead to a spatially oscillating fifth force which is screened in regions of high density via the chameleon mechanism. Consider for a example [7] the chameleon field profile around a spherical object of radius R_c and density $\rho(r)$. The profile of the chameleon field which acts also as a potential for the chameleon fifth force is determined by the equation

$$\frac{d^2\phi}{dr^2} + \frac{2}{r}\frac{d\phi}{dr} = V_{,\phi} + \frac{\beta}{M_{\rm Pl}}\rho(r)e^{\beta\phi/M_{\rm Pl}}, \tag{4.1}$$

where β is a parameter, $M_{\rm Pl}$ is the Planck mass scale and $V(\phi)$ is the chameleon field self-interaction potential. The density profile may be approximated as

$$\rho(r) = \begin{cases} \rho_c & \text{for } r < R_c \\ \rho_\infty & \text{for } r > R_c \end{cases}. \tag{4.2}$$

Let ϕ_c and ϕ_∞ be the chameleon field value that minimizes the effective potential $V_{\rm eff}$ defined as $V_{\rm eff}(\phi) \equiv V(\phi) + \rho(r)e^{\beta_i\phi/M_{\rm Pl}}$ for $r < R_c$ and $r > R_c$, respectively. For these field values we have [7]

$$\begin{aligned} V_{,\phi}(\phi_c) + \frac{\beta}{M_{\rm Pl}}\rho_c e^{\beta\phi_c/M_{\rm Pl}} &= 0 \\ V_{,\phi}(\phi_\infty) + \frac{\beta}{M_{\rm Pl}}\rho_\infty e^{\beta\phi_\infty/M_{\rm Pl}} &= 0. \end{aligned} \tag{4.3}$$

The screened chameleon fifth force is obtained from the profile solution of Eq. (4.1) with boundary conditions

$$\begin{aligned} \frac{d\phi}{dr} &= 0 \quad \text{at } r = 0 \\ \phi &\to \phi_\infty \quad \text{as } r \to \infty. \end{aligned} \tag{4.4}$$

It can be shown from the chameleon field action that the chameleon fifth force on a test particle of mass M is of the form

$$\vec{F}_\phi = -\frac{\beta}{M_{\rm Pl}} M\vec{\nabla}\phi. \quad (4.5)$$

Thus ϕ plays the role a potential for the chameleon induced fifth force.

If the chameleon self-interaction potential is monotonic between the central value ϕ_c and the asymptotic field value ϕ_∞ then $\phi(r)$ varies monotonically between its value ϕ_c in the center of the massive object and its asymptotic value ϕ_∞ which is approached exponentially fast in the exterior of the massive body. We thus obtain the usual screened fifth force obtained from the gradient of $\phi(r)$ which is maximized around a thin shell at the borderline of the massive object and goes rapidly to 0 in the intrerior and in the exterior of the object with significantly larger mass in the interior (screened region).

If on the other hand there are multiple extrema of the potential $V(\phi)$ in the range between the central value ϕ_c and the asymptotic field value ϕ_∞, then Eq. (4.1) implies that these extrema may be inherited to the chameleon field profile around the massive object. Thus from Eq. (4.5) these multiple extrema may induce localized sub-mm spatial oscillations of the chameleon induced screened fifth force. A similar behavior may be obtained if the exponential conformal coupling to the density $e^{\beta\phi/M_{\rm Pl}}$ is replaced by an oscillating function. The detailed investigation of this class of fifth forces and their signature in the SOLME data is an interesting extension of the present project.

The numerical analysis Mathematica files used for the construction of the figures and the derivations of the source integrals may be found at Ref. [84].

ACKNOWLEDGMENTS

We thank the authors of Ref. [32] and especially Professor David Moore and Professor Giorgio Gratta for providing their data set, for confirming the presence of the detected signal in their data and for useful comments regarding the possible origin of this oscillating signal.

APPENDIX NUMERICAL ANALYSIS

In Table I we show the data set used in our maximum likelihood analysis. The data set includes the distance between the center of the microsphera and the origin of a cartesian coordinate system which located in the center of the front side of the cantilever (see Fig. 1 of [32]), the residual force (the difference between the measured force F and the electrostatic background F_B), the corresponding 1σ error and the number of the experiment (microsphera). The data set was kindly provided by the authors of Ref. [32]) after our request.

TABLE I. The residual force 96 data points used for the χ^2 analysis.

$r(\mu m)$	$F-F_B$ (fN)	$1\sigma(F-F_B)$	Microsphera
26.2	−0.0098	0.017	I
36.2	0.0193	0.0235	I
46.2	0.0373	0.0355	I
56.2	−0.0301	0.0359	I
66.2	0.0445	0.0572	I
66.4	−0.0186	0.0219	I
76.2	−0.0248	0.0762	I
76.4	0.019	0.0205	I
86.2	0.0461	0.0504	I
86.4	0.0363	0.0218	I
96.2	−0.035	0.0173	I
96.4	−0.0055	0.0183	I
102.4	−0.0152	0.0166	I
106.4	0.027	0.016	I
112.4	0.0248	0.0165	I
116.4	0.038	0.016	I
122.4	−0.0178	0.0158	I
126.4	−0.0557	0.0171	I
132.4	0.0017	0.0165	I
136.4	−0.0123	0.0195	I
142.4	0.0114	0.0164	I
152.4	0.007	0.0158	I
158.5	−0.0012	0.0162	I
162.4	−0.0169	0.0193	I
168.5	0.0061	0.0156	I
172.4	0.0133	0.0165	I
178.5	−0.0005	0.0156	I
188.5	0.0016	0.0155	I
198.5	−0.0095	0.0202	I
208.5	0.0048	0.0175	I
218.5	−0.0163	0.0183	I
228.5	−0.0075	0.0162	I
25.3	−0.0439	0.0565	II
35.3	0.0398	0.0321	II
45.3	0.0217	0.0325	II
55.3	−0.0271	0.0344	II
64.9	0.0124	0.0593	II
65.3	0.0189	0.0358	II
74.9	−0.0605	0.042	II
75.3	−0.0388	0.0244	II
84.9	0.0116	0.0341	II
85.3	−0.0395	0.0184	II
94.9	−0.0045	0.0364	II
95.3	0.0185	0.0397	II
104.9	0.0237	0.0213	II
106.1	−0.0083	0.0185	II
114.9	−0.0044	0.0271	II
116.1	0.0482	0.0183	II
124.9	−0.0175	0.0249	II
126.1	−0.0149	0.02	II
134.9	0.0064	0.0222	II
136.1	−0.0167	0.0309	II
146.1	0.0176	0.041	II
156.1	0.0072	0.0351	II

(Table continued)

TABLE I. *(Continued)*

$r(\mu m)$	$F - F_B$ (fN)	$1\sigma(F - F_B)$	Microsphera
159.1	0.0478	0.0211	II
166.1	0.0193	0.033	II
169.1	−0.009	0.0213	II
176.1	0.015	0.0195	II
179.1	0.0029	0.0206	II
189.1	−0.0225	0.0209	II
199.1	0.0107	0.0218	II
209.1	−0.0238	0.0233	II
219.1	0.0032	0.0233	II
229.1	−0.0158	0.0202	II
25.8	0.0012	0.0383	III
35.8	−0.0074	0.0579	III
45.8	0.001	0.0402	III
55.8	−0.0469	0.0461	III
63.9	−0.0123	0.0149	III
65.8	−0.0053	0.0196	III
73.9	−0.0055	0.0143	III
75.8	0.0015	0.02	III
83.9	0.0266	0.0314	III
85.8	−0.0247	0.0143	III
93.9	−0.0018	0.0163	III

(Table continued)

TABLE I. *(Continued)*

$r(\mu m)$	$F - F_B$ (fN)	$1\sigma(F - F_B)$	Microsphera
95.8	0.0366	0.0206	III
103.9	0.0316	0.0167	III
108.	0.0369	0.0153	III
113.9	0.0105	0.0168	III
118.	0.0041	0.0183	III
123.9	−0.0025	0.0163	III
128.	0.0158	0.0385	III
133.9	−0.001	0.0269	III
138.	−0.0173	0.0317	III
148.	0.0098	0.0264	III
158.	−0.0233	0.0258	III
164.6	−0.0042	0.0212	III
168.	−0.0193	0.0146	III
174.6	−0.014	0.0215	III
178.	0.0059	0.0136	III
184.6	−0.0178	0.0267	III
194.6	−0.0011	0.0257	III
204.6	−0.02	0.0298	III
214.6	−0.0008	0.0309	III
224.6	−0.0015	0.0222	III
234.6	−0.0305	0.0204	III

[1] P. Brax, C. van de Bruck, A.-C. Davis, J. Khoury, and A. Weltman, Detecting dark energy in orbit: The Cosmological chameleon, Phys. Rev. D **70**, 123518 (2004).

[2] J. Khoury and A. Weltman, Chameleon Fields: Awaiting Surprises for Tests of Gravity in Space, Phys. Rev. Lett. **93**, 171104 (2004).

[3] P. Brax, C. van de Bruck, A.-C. Davis, and D. J. Shaw, $f(R)$ Gravity and chameleon theories, Phys. Rev. D **78**, 104021 (2008).

[4] R. Gannouji, B. Moraes, D. F. Mota, D. Polarski, S. Tsujikawa, and H. A. Winther, Chameleon dark energy models with characteristic signatures, Phys. Rev. D **82**, 124006 (2010).

[5] J. Khoury, Chameleon Field Theories, Classical Quantum Gravity **30**, 214004 (2013).

[6] C. Burrage and J. Sakstein, A Compendium of Chameleon Constraints, J. Cosmol. Astropart. Phys. 11 (2016) 045.

[7] J. Khoury and A. Weltman, Chameleon cosmology, Phys. Rev. D **69**, 044026 (2004).

[8] I. Antoniou, Constraints on scalar coupling to electromagnetism, Gravitation Cosmol. **23**, 171 (2017).

[9] K. Koyama, Cosmological tests of modified gravity, Rep. Prog. Phys. **79**, 046902 (2016).

[10] S. Rahvar and B. Mashhoon, Observational tests of nonlocal gravity: Galaxy rotation curves and clusters of galaxies, Phys. Rev. D **89**, 104011 (2014).

[11] M. Bordag, U. Mohideen, and V. M. Mostepanenko, New developments in the Casimir effect, Phys. Rep. **353**, 1 (2001).

[12] G. L. Klimchitskaya, U. Mohideen, and V. M. Mostepanenko, The Casimir force between real materials: Experiment and theory, Rev. Mod. Phys. **81**, 1827 (2009).

[13] K. A. Milton, The Casimir effect: Recent controversies and progress, J. Phys. A **37**, R209 (2004).

[14] D. J. Kapner, T. S. Cook, E. G. Adelberger, J. H. Gundlach, Blayne R. Heckel, C. D. Hoyle, and H. E. Swanson, Tests of the Gravitational Inverse-Square Law Below the Dark-Energy Length Scale, Phys. Rev. Lett. **98**, 021101 (2007).

[15] E. Fischbach and C. L. Talmadge, *The Search for Non-Newtonian Gravity* (Springer-Verlag, New York, 1999).

[16] E. G. Adelberger, B. R. Heckel, C. W. Stubbs, and W. F. Rogers, Searches for new macroscopic forces, Annu. Rev. Nucl. Part. Sci. **41**, 269 (1991).

[17] E. G. Adelberger, B. R. Heckel, and A. E. Nelson, Tests of the gravitational inverse square law, Annu. Rev. Nucl. Part. Sci. **53**, 77 (2003).

[18] J. Chiaverini, S. J. Smullin, A. A. Geraci, D. M. Weld, and A. Kapitulnik, New Experimental Constraints on Non-Newtonian Forces Below 100 μm, Phys. Rev. Lett. **90**, 151101 (2003).

[19] J. C. Long, H. W. Chan, A. B. Churnside, E. A. Gulbis, M. C. M. Varney, and J. C. Price, Upper limits to submillimeter-range

forces from extra space-time dimensions, Nature (London) **421**, 922 (2003).
[20] J. K. Hoskins, R. D. Newman, R. Spero, and J. Schultz, Experimental tests of the gravitational inverse square law for mass separations from 2 to 105 cm, Phys. Rev. D **32**, 3084 (1985).
[21] R. Spero, J. K. Hoskins, R. Newman, J. Pellam, and J. Schultz, Test of the Gravitational Inverse-Square Law at Laboratory Distances, Phys. Rev. Lett. **44**, 1645 (1980).
[22] M. V. Moody and H. J. Paik, Gauss's Law Test of Gravity at Short Range, Phys. Rev. Lett. **70**, 1195 (1993).
[23] K. Kuroda and H. Hirakawa, Experimental test of the law of gravitation, Phys. Rev. D **32**, 342 (1985).
[24] H. A. Chan, M. V. Moody, and H. J. Paik, Null Test of the Gravitational Inverse Square Law, Phys. Rev. Lett. **49**, 1745 (1982).
[25] E. G. Adelberger, J. H. Gundlach, B. R. Heckel, S. Hoedl, and S. Schlamminger, Torsion balance experiments: A low-energy frontier of particle physics, Prog. Part. Nucl. Phys. **62**, 102 (2009).
[26] S. J. Smullin, A. A. Geraci, D. M. Weld, J. Chiaverini, S. P. Holmes, and A. Kapitulnik, New constraints on Yukawa-type deviations from Newtonian gravity at 20 microns, Phys. Rev. D **72**, 122001 (2005); New constraints on Yukawa-type deviations from Newtonian gravity at 20 microns, Phys. Rev. D **72**, 129901(E) (2005).
[27] A. A. Geraci, S. J. Smullin, D. M. Weld, J. Chiaverini, and A. Kapitulnik, Improved constraints on non-Newtonian forces at 10 microns, Phys. Rev. D **78**, 022002 (2008).
[28] K. Ninomiya *et al.*, Short-range test of the universality of gravitational constant G at the millimeter scale using a digital image sensor, arXiv:1708.01482 [Classical Quantum Gravity (to be published)].
[29] S. K. Lamoreaux, Demonstration of the Casimir Force in the 0.6 to 6 μm Range, Phys. Rev. Lett. **78**, 5 (1997); Demonstration of the Casimir Force in the 0.6 to 6 μm Range, Phys. Rev. Lett. **81**, 5475(E) (1998).
[30] A. O. Barvinsky, Dark energy and dark matter from nonlocal ghost-free gravity theory, Phys. Lett. B **710**, 12 (2012).
[31] G. L. Klimchitskaya and V. M. Mostepanenko, Constraints on axionlike particles and non-Newtonian gravity from measuring the difference of Casimir forces, Phys. Rev. D **95**, 123013 (2017).
[32] A. D. Rider, D. C. Moore, C. P. Blakemore, M. Louis, M. Lu, and G. Gratta, Search for Screened Interactions Associated with Dark Energy Below the 100 μm Length Scale, Phys. Rev. Lett. **117**, 101101 (2016).
[33] T. Li, S. Kheifets, and M. G. Raizen, Millikelvin cooling of an optically trapped microsphere in vacuum, Nat. Phys. **7**, 527 (2011).
[34] A. A. Geraci, S. B. Papp, and J. Kitching, Short-Range Force Detection Using Optically Cooled Levitated Microspheres, Phys. Rev. Lett. **105**, 101101 (2010).
[35] D. C. Moore, A. D. Rider, and G. Gratta, Search for Millicharged Particles Using Optically Levitated Microspheres, Phys. Rev. Lett. **113**, 251801 (2014).
[36] J. Wang, S. Guan, K. Chen, W. Wu, Z. Tian, P. Luo, A. Jin, S. Yang, C. Shao, and J. Luo, Test of non-Newtonian gravitational forces at micrometer range with two-dimensional force mapping, Phys. Rev. D **94**, 122005 (2016).
[37] P. Brax and A.-C. Davis, Atomic interferometry test of dark energy, Phys. Rev. D **94**, 104069 (2016).
[38] A. Hees *et al.*, Testing General Relativity with Stellar Orbits around the Supermassive Black Hole in our Galactic Center, Phys. Rev. Lett. **118**, 211101 (2017).
[39] E. G. Adelberger, B. R. Heckel, S. A. Hoedl, C. D. Hoyle, D. J. Kapner, and A. Upadhye, Particle Physics Implications of a Recent Test of the Gravitational Inverse Sqaure Law, Phys. Rev. Lett. **98**, 131104 (2007).
[40] L. Perivolaropoulos, PPN parameter γ and solar system constraints of massive Brans-Dicke theories, Phys. Rev. D **81**, 047501 (2010).
[41] M. Hohmann, L. Jarv, P. Kuusk, and E. Randla, Post-Newtonian parameters γ and β of scalar-tensor gravity with a general potential, Phys. Rev. D **88**, 084054 (2013); Post-Newtonian parameters γ and β of scalar-tensor gravity with a general potential, Phys. Rev. D **89**, 069901(E) (2014).
[42] L. Järv, P. Kuusk, M. Saal, and O. Vilson, Invariant quantities in the scalar-tensor theories of gravitation, Phys. Rev. D **91**, 024041 (2015).
[43] S. Nojiri and S. D. Odintsov, Newton potential in de Sitter brane world, Phys. Lett. B **548**, 215 (2002).
[44] A. Donini and S. G. Marimón, Micro-orbits in a many-brane model and deviations from Newton's $1/r^2$ law, Eur. Phys. J. C **76**, 696 (2016).
[45] R. Benichou and J. Estes, The fate of Newton's law in brane-world scenarios, Phys. Lett. B **712**, 456 (2012).
[46] K. A. Bronnikov, S. A. Kononogov, and V. N. Melnikov, Brane world corrections to Newton's law, Gen. Relativ. Gravit. **38**, 1215 (2006).
[47] B. Guo, Y.-X. Liu, and K. Yang, Brane worlds in gravity with auxiliary fields, Eur. Phys. J. C **75**, 63 (2015).
[48] M. Kaminski, K. Landsteiner, J. Mas, J. P. Shock, and J. Tarrio, Holographic operator mixing and quasinormal modes on the brane, J. High Energy Phys. 02 (2010) 021.
[49] C. P. L. Berry and J. R. Gair, Linearized $f(R)$ gravity: Gravitational radiation and Solar System tests, Phys. Rev. D **83**, 104022 (2011); Linearized $f(R)$ gravity: Gravitational radiation and Solar System tests, Phys. Rev. D **85**, 089906(E) (2012).
[50] S. Capozziello, A. Stabile, and A. Troisi, A general solution in the Newtonian limit of f(R)-gravity, Mod. Phys. Lett. A **24**, 659 (2009).
[51] G. O. Schellstede, On the Newtonian limit of metric f(R) gravity, Gen. Relativ. Gravit. **48**, 118 (2016).
[52] N. Arkani-Hamed, S. Dimopoulos, and G. R. Dvali, The hierarchy problem and new dimensions at a millimeter, Phys. Lett. **B429**, 263 (1998).
[53] N. Arkani-Hamed, S. Dimopoulos, and G. R. Dvali, Phenomenology, astrophysics and cosmology of theories with submillimeter dimensions and TeV scale quantum gravity, Phys. Rev. D **59**, 086004 (1999).
[54] I. Antoniadis, N. Arkani-Hamed, S. Dimopoulos, and G. R. Dvali, New dimensions at a millimeter to a Fermi and superstrings at a TeV, Phys. Lett. B **436**, 257 (1998).
[55] L. Perivolaropoulos and C. Sourdis, Cosmological effects of radion oscillations, Phys. Rev. D **66**, 084018 (2002).

[56] E. G. Floratos and G. K. Leontaris, Low scale unification, Newton's law and extra dimensions, Phys. Lett. B **465**, 95 (1999).
[57] A. Kehagias and K. Sfetsos, Deviations from the $1/r^2$ Newton law due to extra dimensions, Phys. Lett. B **472**, 39 (2000).
[58] I. Antoniadis, An introduction to extra dimensions and sting phenomenology, *Proc. Sci.*, CORFU2015 (2016) 007.
[59] D. F. Mota and D. J. Shaw, Strongly Coupled Chameleon Fields: New Horizons in Scalar Field Theory, Phys. Rev. Lett. **97**, 151102 (2006).
[60] C. Burrage, E. J. Copeland, and E. A. Hinds, Probing dark energy with atom interferometry, J. Cosmol. Astropart. Phys. 03 (2015) 042.
[61] B. Elder, J. Khoury, P. Haslinger, M. Jaffe, H. Müller, and P. Hamilton, Chameleon dark energy and atom interferometry, Phys. Rev. D **94**, 044051 (2016).
[62] L. Perivolaropoulos, Submillimeter spatial oscillations of Newton's constant: Theoretical models and laboratory tests, Phys. Rev. D **95**, 084050 (2017).
[63] J. Edholm, A. S. Koshelev, and A. Mazumdar, Behavior of the Newtonian potential for ghost-free gravity and singularity-free gravity, Phys. Rev. D **94**, 104033 (2016).
[64] A. Conroy, T. Koivisto, A. Mazumdar, and A. Teimouri, Generalized quadratic curvature, nonlocal infrared modifications of gravity and Newtonian potentials, Classical Quantum Gravity **32**, 015024 (2015).
[65] A. Conroy and J. Edholm, Newtonian potential and geodesic completeness in infinite derivative gravity, Phys. Rev. D **96**, 044012 (2017).
[66] P. Burikham, T. Harko, and M. J. Lake, The QCD mass gap and quark deconfinement scales as mass bounds in strong gravity arXiv:1705.11174.
[67] M. J. Lake, Is there a connection between "dark" and "light" physics?, J. Phys. Conf. Ser. **883**, 012001 (2017).
[68] L. Modesto and L. Rachwal, Nonlocal quantum gravity: A review, Int. J. Mod. Phys. D **26**, 1730020 (2017).
[69] L. Amendola, N. Burzilla, and H. Nersisyan, Quantum gravity inspired nonlocal gravity model, arXiv:1707.04628 [Phys. Rev. D (to be published)].
[70] A. Conroy, Ph. D. thesis, Lancaster University, 2017 [arXiv:1704.07211].
[71] A. S. Koshelev and A. Mazumdar, Absence of event horizon in massive compact objects in infinite derivative gravity, arXiv:1707.00273.
[72] G. Calcagni and L. Modesto, Stability of Schwarzschild singularity in nonlocal gravity, Phys. Lett. B **773**, 596 (2017).
[73] S. Talaganis and A. Teimouri, Hamiltonian analysis for infinite derivative field theories and gravity, arXiv:1701.01009.
[74] L. Buoninfante, Ghost and singularity free theories of gravity, arXiv:1610.08744.
[75] B. L. Giacchini, On the cancellation of Newtonian singularities in higher-derivative gravity, Phys. Lett. B **766**, 306–311 (2017).
[76] A. Accioly, B. L. Giacchini, and I. L. Shapiro, On the gravitational seesaw in higher-derivative gravity, Eur. Phys. J. C **77**, 540 (2017).
[77] Y. Dirian, S. Foffa, M. Kunz, M. Maggiore, and V. Pettorino, Nonlocal gravity and comparison with observational data sets, J. Cosmol. Astropart. Phys. 04 (2015) 044.
[78] Y. Dirian, S. Foffa, M. Kunz, M. Maggiore, and V. Pettorino, Nonlocal gravity and comparison with observational data sets. II. Updated results and Bayesian model comparison with ΛCDM, J. Cosmol. Astropart. Phys. 05 (2016) 068.
[79] M. Maggiore and M. Mancarella, Nonlocal gravity and dark energy, Phys. Rev. D **90**, 023005 (2014).
[80] V. Vardanyan, Y. Akrami, L. Amendola, and A. Silvestri, On nonlocally interacting metrics, and a simple proposal for cosmic acceleration, arXiv:1702.08908.
[81] S. Park and A. Shafieloo, Growth of perturbations in nonlocal gravity with non-ΛCDM background, Phys. Rev. D **95**, 064061 (2017).
[82] L. Feng, Light bending in infinite derivative theories of gravity, Phys. Rev. D **95**, 084015 (2017).
[83] A. D. Rider, D. C. Moore, C. P. Blakemore, M. Louis, M. Lu, and G. Gratta (private communication).
[84] http://leandros.physics.uoi.gr/solme/.